J. Fluid Mech. (2002), *vol.* 469, *pp.* 49–70.
DOI: 10.1017/S0022112002001672 Printed in the United Kingdom

Entrainment vortices and interfacial intermittent turbulent bulges in a plane turbulent wake

By GREGORY A. KOPP[1], FRANCESC GIRALT[2] AND JAMES F. KEFFER[3]†

[1]Boundary Layer Wind Tunnel Laboratory, Faculty of Engineering, University of Western Ontario, London, Ontario, N6A 5B9, Canada

[2]Department d'Enginyeria Química, ETSEQ, Universitat Rovira i Virgili, Campus Sescelades, Av. dels Països Catalans, 26, 43007 Tarragona, Catalunya, Spain

[3]Department of Mechanical and Industrial Engineering, University of Toronto, 5 King's College Road, Toronto. Ontario, M5S 1A4, Canada

(Received 5 October 2000 and in revised form 13 May 2002)

Hot-wire measurements were made simultaneously in two homogeneous 'horizontal' planes in the far-wake region of a cylinder. A technique developed using hot-wire data to identify the spatial characteristics of the large-scale bulges at the interface between the internal turbulent motions and the external irrotational flow was used to unambiguously relate these outer intermittent bulges to the inner coherent structures. It was found that a turbulent bulge is made up of a combination of a horseshoe vortex (whose legs form one double-roller eddy) and the straining region present just upstream of this structure. The approach also allowed the evaluation of the two most prominent phenomenological models for the entrainment mechanism in the far-wake region: the Kelvin–Helmholtz instability and Townsend's growth–decay cycle. It was found that the decaying and re-forming of the bulges and entrainment structures is not likely to occur. Rather, the evidence is that the large-scale bulges remain coherent for long streamwise distances in equilibrium with the overall similarity of the flow.

1. Introduction

Understanding the kinematics and dynamics of entrainment and mixing is important in many practical engineering situations such as the dispersion of contaminants or combustion. In these applications, flows tend to be complex and many engineering turbulence models used to predict them break down. The fundamental study of three-dimensional turbulence structures and their related transfer processes in the far region of a plane turbulent wake is relevant to these situations because entrainment and the transfer of momentum, heat and mass that occur in free flows depend strongly on the structure of the internal vortical motions and how these motions interact with the external 'irrotational' flow field.

Turbulent mixing takes place in three stages. The first is the process of entrainment whereby the exterior irrotational fluid is ingested by the interior rotational turbulent flow. This process, sometimes called engulfment, involves the extension of the interface separating the irrotational and rotational flow by large-scale turbulent motions. Dimotakis (2000) refers to the second stage as 'stirring', where the interface between the species being mixed grows at scales smaller than the large scales responsible for

† Adjunct Professor to the doctorate programme at the Universitat Rovira i Virgili.

engulfing, but larger than the viscous scales. In the final stage, molecular mixing smooths out the gradients of the different species.

Overall rates of entrainment and mixing are controlled by the large structures (e.g. Townsend 1976; Bevilaqua & Lykoudis 1977) and, as such, are boundary- and initial-condition dependent (Wygnanski, Champagne & Marasli 1986). There has been much work focused on the identification of the bulges (e.g. Corrsin & Kistler 1955; Hedley & Keffer 1974; LaRue & Libby 1976) and coherent structures (e.g. Mumford 1983; Antonia *et al.* 1987; Ferré & Giralt 1989*a*, *b*). Extensive work has also been done to define the geometry and phenomenology of folding of the interface, that is, the stirring process (e.g. Ottino 1989; Sreenivasan 1991; Villermaux & Innocenti 1999; Catrakis & Bond 2000).

Recent work has shown very interesting interactions between the large-scale entraining eddies and the small-scale motions, particularly with regard to entraining and mixing of passive scalars. It was traditionally argued (e.g. Townsend 1966) that the largest eddies interacted with the next smaller size, these then with the next smaller and so on, in an energy cascade. As discussed in Warhaft (2000), for example, a mean temperature gradient aligned with diverging–converging separatrices (i.e. large-scale motions) yields the ramp–cliff structures that are associated with the anisotropy of the small scales of a passive scalar. Thus, there is a more direct interaction between the large and small scales than previously thought.

There have been two phenomenological descriptions of the entrainment mechanism in the literature, the most common being the roll-up due to Kelvin–Helmholtz (KH) instability. This instability causes a vortex sheet to roll up (e.g. Prandtl & Tietjens 1934; Sreenivasan, Ramshankar & Meneveau 1989; Caulfield & Peltier 2000), entrapping external non-turbulent fluid all the way into the core of the vortex (e.g. see figure 4 in Sreenivasan *et al.* 1989) and yielding the well-known 'cat's eye' streamline pattern. This description has been used primarily to portray engulfment in the near and intermediate wake regions where the vortex street is still reasonably strong and periodic.

Townsend's (1966, 1976) growth–decay model, illustrated on the cover of his book, consists of a cycle of entrainment applicable in the far-wake region, which begins with a quiescent period characterized by a relatively smooth interface in the large-scale sense. This is followed by a period of growth of packets, which become the large bulges that eventually overturn, engulfing a large amount of external fluid. As a result, the wake approximately doubles its size by the end of this cycle. Once the overturning is complete, the interface becomes quiescent again and the cycle begins again.

The growth–decay model is closely related to the KH instability. In both cases, the engulfment structures originate out of a nearly smooth interface and are formed because of the instability of the mean velocity profile. The major difference appears to be that in Townsend's model, when the structures overturn they are destroyed, leading to the next quiescent period. This appears to be like a breaking wave, as noted by Bevilaqua & Lykoudis (1977). Aside from this, the similarity between the KH instability and the growth–decay cycle is striking.

In contrast to the KH instability mechanism and the growth–decay cycle, Bevilaqua & Lykoudis (1977) proposed that rotational motions 'sweep' non-turbulent fluid into the turbulent region. They proposed this mechanism based on experiments where they injected dye into the external stream and observed how it was entrained. They also observed that the large structures were long-lasting. Recently, Sreenivas & Prasad (2000) reported that a similar type of mechanism occurs in the far field of plane jets (although they gave no evidence of this). This appears to us more as a difference in

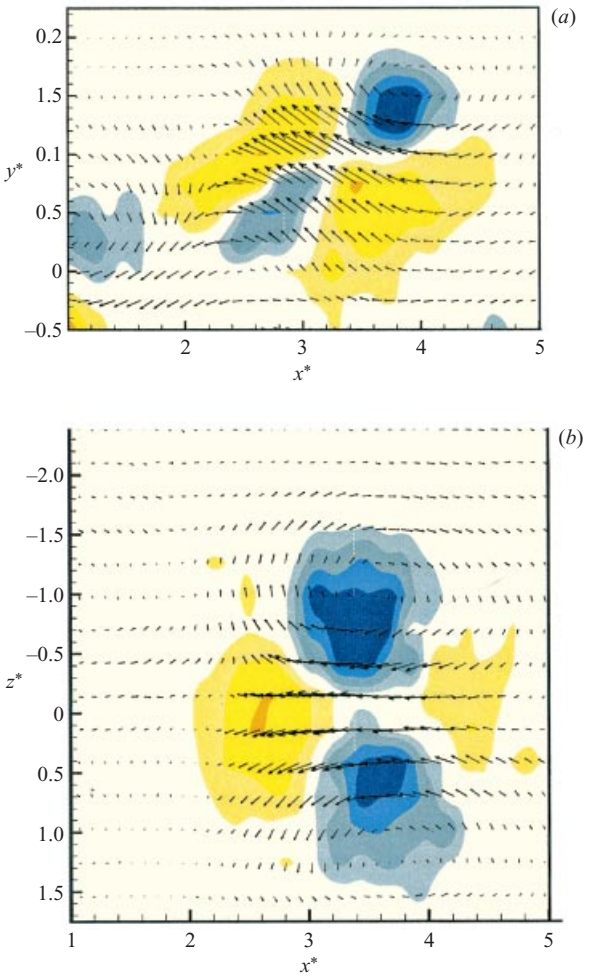

FIGURE 1. The velocity maps in (*a*) the (x^*, y^*)-plane at $z^* = 0$ for (u_c^*, v_c^*), and (*b*) the (x^*, z^*)-plane at $y^* = 1$ for (u_c^*, w_c^*), from Vernet *et al.* (1999). Contours are of the second invariant: the yellow colours indicate regions where strain dominates while the blue colours indicate regions where rotation does so. The lowest isocontours are for 5% of the maximum value of the second invariant.

degree than of mechanism. In the near wake, the Kármán vortices account for large fractions of the total fluctuation energy and rotate relatively rapidly so entrained fluid can get near the core of the vortex quickly, before it becomes fully turbulent. In the far wake, however, the horseshoe vortices themselves account for much smaller fractions of the total energy and do not rotate rapidly enough so that the entrainment fluid can become turbulent before reaching the core (see also Vernet *et al.* 1999).

Vernet *et al.* (1999) identified the complete three-dimensional topology of the large-scale structure in the far region of a cylinder wake. Figure 1 shows the ensemble-averaged velocity fluctuation maps and the second invariant calculated from the data measured by these authors. In this figure the flow is from left to right. The isosurfaces of the second invariant, Q, of the coherent field

$$Q \equiv \tfrac{1}{2}(u_{c,i,j}^2 - u_{c,i,j}\ u_{c,j,i}) = -\tfrac{1}{2}u_{c,i,j}\ u_{c,j,i} = \tfrac{1}{2}(\|\Omega_c\|^2 - \|S_c\|^2) \qquad (1)$$

were obtained from a triple decomposition (where c is not an index but denotes

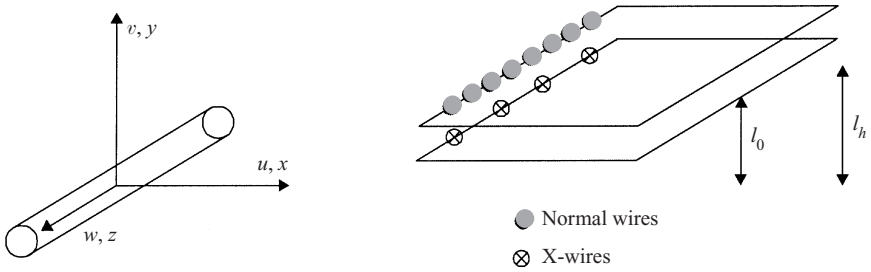

FIGURE 2. Definition sketch of the experimental set-up.

the coherent motions) to identify regions within the structure where rotation or straining dominates. As indicated by Giralt & Ferré (1993), the well-known double-roller structure (or pair of counter-rotating vortices) is simply a horizontal slice through a horseshoe vortex near the wake half-width (i.e. $y \sim l_0$) as can be inferred from figure 1(*b*). Grant's (1958) mixing jets should be associated with the strong outward velocities with negative streamwise fluctuations seen in figure 1(*a*). What is particularly interesting is that there is a clear shear alignment of both the upstream straining region (in yellow) and the rotational region (in blue). The downstream straining region does not show the same alignment with the mean shear on its lower edge. However, when a double decomposition is applied, as was done by Antonia, Shah & Browne (1987), the shear alignment of the contours disappear and they are all closer to the wake centreline. LaRue & Libby (1976) found that the upstream edge of the bulges tend to be shear aligned while the downstream edge does not. As a consequence, the possibility that the bulges are made up of these straining and rotational regions deserves further investigation.

In this paper we present a conditional-averaging technique to identify the large-scale turbulent bulges. Data obtained simultaneously in two homogenous horizontal planes are used to position the (outer) bulges, along with the quiescent irrotational zones, relative to the (inner) coherent structures. The details of the entrainment mechanism are evaluated and clarified by examining the characteristics and topology of the bulges and coherent structures simultaneously. These are then related to the overall growth and similarity of the wake.

2. Details of experiments and analysis

2.1. *Description of experiments*

Measurements were made in a plane turbulent cylinder wake generated in the open return wind tunnel of the Chemical Engineering Department at the Universitat Rovira i Virgili in Tarragona. This facility has a test section 60×60 cm square and 300 cm long. The diameter of the cylinder, D, was 11.6 mm (aspect ratio of 40 and tunnel blockage of 2.0%) while the free-stream velocity, U_0, was 9 m s^{-1}, so that the Reynolds number was 6700. The cylinder was mounted through holes in the tunnel walls. The free-stream turbulence intensity was less than 0.2%.

Figure 2 shows a sketch of the setup. A moveable rake of 4 X-wires was placed 170 diameters downstream of the cylinder to measure the (u, w) velocity components. This rake could be moved between the centreline and $y = l_0$, where l_0 is the mean velocity half-width. The probe spacing was $\Delta z = 0.33 l_0$ in order to capture the large-scale features of the inner-wake flow coherent structures. A second fixed rake of 8 normal

wires was placed immediately above the X-wire rake near the half-intermittency point ($y = l_h$) in order to sense the interface between the turbulent and the irrotational flow and measure the streamwise velocity components there. The probe spacing for the normal wire rake was $\Delta z = 0.14 l_0$, so that both rakes had the same spanwise extent. The voltage signals from each anemometer were sampled at 5 kHz per channel for 40 s ($\Delta t = 0.2$ ms), low-pass filtered at 2 kHz, and stored on disk.

There are several additional points to note. First, the spatial coordinates are normalized according to $z^* = z/l_0$, $y^* = y/l_0$, and $x^* = -U_0 t/l_0$ (assuming Taylor's hypothesis) while velocities are normalized as $u^* = u/u_0$, $v^* = v/u_0$ and $w^* = w/u_0$ where u_0 is the maximum velocity defect. A prime ($'$) denotes an r.m.s. component, a single overbar a time average and a double overbar a spatial average. Second, flow is from left to right in all plots. Third, the mean velocity half-width length scale was $l_0 = 42$ mm, the half-intermittency point was located at $y = l_h = 1.65 l_0$ and the integral scale, L, calculated from the streamwise autocorrelation, was 3.2 ms ($\approx 0.7 l_0$, assuming Taylor's hypothesis). Finally, although the Reynolds number based on the Taylor microscale, $Re_\lambda = u' \lambda_T / \nu$, was 110, both the turbulence and mixing are not likely to be fully developed since $Re_D \lesssim 10\,000$ (Dimotakis 2000). This could have an effect on the smaller scales of turbulence although it is not expected to have a large effect at the scales examined in this work.

2.2. *Decomposition and averaging techniques*

Double and triple decompositions of the velocity field (e.g. Hussain 1983) have been applied to identify coherent structures embedded in turbulent flows. In the present work, the triple decomposition is used. The triple decomposition decomposes the total instantaneous velocity, u, as the sum of the mean, $\overline{U}$, the coherent, u_c, and an incoherent fluctuation, u_r,

$$u_i(x, y, z, t) = \overline{U_i}(x, y) + u_{c,i}(x, y, z, t) + u_{r,i}(x, y, z, t). \tag{2}$$

The coherent velocity, u_c, is the ensemble average of the difference between the total and mean velocities, i.e. $u_c = \langle u - \overline{U} \rangle$ (e.g. Hussain 1983; Antonia *et al.* 1987). The angular brackets indicate the ensemble average, the subscripts c and r identify the coherent and incoherent components, and the index, i, represents the three coordinate directions.

In the present work, the x-dependence has not been explicitly measured. Rather, we have relied on Taylor's hypothesis to convert the time-based measurements into spatial x. The assumption of Taylor's hypothesis implies that structures do not change as they pass the set of probes. This also means that the explicit time dependence of the structures is not a factor if all structures included in the average are roughly of the same 'age'.

2.3. *Turbulence indicator function*

The turbulence indicator function,

$$I(x, y, z, t) = \begin{cases} 1, & \text{turbulent} \\ 0, & \text{otherwise,} \end{cases} \tag{3}$$

is the time history of the turbulent–non-turbulent interface at position (x, y, z). Since turbulence is characterized by random vorticity fluctuations, identification of the interface separating turbulent and non-turbulent (irrotational) fluid domains would be best accomplished via the instantaneous vorticity signal because there are effectively zero levels of random vorticity in the free stream and non-zero levels within the

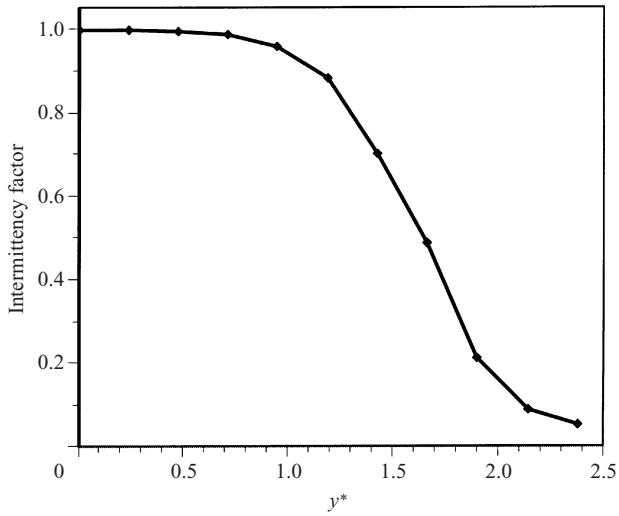

FIGURE 3. Variation of the intermittency factor at $x/D = 170$.

turbulent flow. Obtaining the random vorticity signal, however, requires the use of special multi-sensor probes, which in the present work would severely limit the investigation of the instantaneous spatial distribution of the interface. Thus, the identification of turbulent zones was made by using the streamwise velocity component obtained from a normal wire, as has been done by numerous researchers (e.g. Corrsin & Kistler 1995; Hedley & Keffer 1974).

Obtaining the turbulence indicator function from a velocity signal is not straightforward because velocity fluctuations can legitimately occur in both the irrotational and the turbulent domains. Thus, an intermittently turbulent velocity signal needs to be sensitized to the presence of turbulence so that the probability density functions of the turbulent and non-turbulent regions are sufficiently separated (Kawall & Keffer 1980). Typically, detector functions are based on the square of the first or second time derivative of the streamwise velocity. In the present work we have used the detector function of Tabatabai, Kawall & Keffer (1989), namely, $((u - U_0)(\partial u/\partial t))^2$. Other functions include that used by Hedley & Keffer (1974), namely $(\partial u/\partial t)^2 + (\partial v/\partial t)^2$. Kawall & Keffer (1980) discussed some of the additional difficulties with detector functions. In the present work, a hold-time, $T_s = 0.6\,\text{ms} \approx 5.4\,\text{mm}$ (assuming Taylor's hypothesis; cf. probe spacing of 6.0 mm) was applied. Thus, the difference in the time and spatial resolution is small. This is consistent with the low-pass filter frequency of 2 kHz, which translates, assuming Taylor's hypothesis, to 4.5 mm and with the sensor length of 1.25 mm. However, the hold-time is about one order of magnitude larger than the Kolmogorov scale, η.

The intermittency factor, $\bar{I}(x, y, z)$ is the time-average of $I(x, y, z, t)$ and is shown for the present flow in figure 3. The turbulence burst rate, $\bar{f}$, is defined to be the average number of transitions from zero to unity per unit time,

$$\bar{f}(x, y) = \frac{B}{T}, \tag{4}$$

where B is the total number of zero to unity transitions over time T. Twice the value of the turbulence burst rate represents the average number of times that the interface passes the probe per unit time. The average turbulent and non-turbulent zone lengths

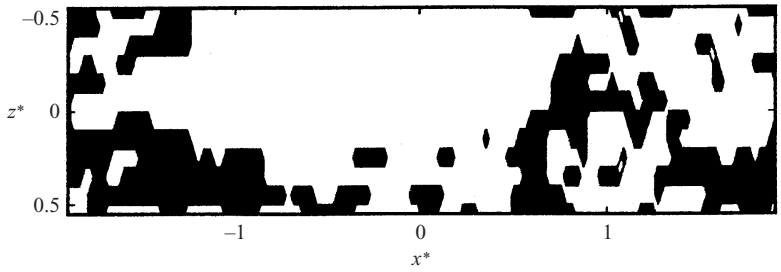

FIGURE 4. A segment of the time series of the turbulence indicator function from the eight normal wires in the (x^*, z^*)-plane at $y^* = 1.7$.

from a single sensor at a single location are defined to be, respectively,

$$\overline{z_t}(x, y) = \frac{1}{B}\sum_{i=1}^{B}(z_t)_i = \frac{\bar{I}(x, y)}{\bar{f}(x, y)}, \quad \overline{z_p}(x, y) = \frac{1 - \bar{I}(x, y)}{\bar{f}(x, y)}. \tag{5}$$

3. Identification of large-scale bulges and non-turbulent zones

3.1. *Identification technique*

The time series of the turbulence indicator functions obtained from the eight normal wires at $y = 1.7l_0 \sim l_h$ were examined. Figure 4 depicts a typical segment of these time series containing a large-scale bulge. The white zones indicate turbulent flow and the black zones indicate non-turbulent flow. It can be observed that there are a few non-turbulent 'patches' surrounded by turbulent flow, implying three-dimensionality of the interface at the downstream end. In addition, at the upstream end of the figure, the interface is generally observed to be continuous, but it undulates significantly. One implicit assumption that should be noted in the plotting of figure 4 is that when two adjacent data points indicated turbulent flow, the spatial locations between the two were assumed to be turbulent also.

Difficulty in the identification of bulges arises if the bulges are assumed to contain any sort of 'porosity', i.e. locations where the intermittency function is zero, indicating the presence of non-turbulent fluid. Since this is the case, as depicted in figure 4 (see also figure 4 in Sreenivasan *et al.* 1989), a threshold is required to determine whether or not any given 'event' is a bulge when identification is performed 'by eye' or automatically. Obviously, small-scale interface undulations are neglected with this approach since this work is not concerned with small-scale measures of the interface (e.g. fractal dimensions).

Several distributions of intermittency occur when sensing the interface with a discrete number of probes. These have to be considered in order to set the appropriate threshold for the turbulence indicator function in the space between adjacent probes. First, if two adjacent probes simultaneously yield long contiguous periods of rotational flow, the only assumption to be made is whether the intervening space is also rotational. A threshold close to unity could be applied in this case. Second, the adjacent probes could yield non-contiguous series of shorter bursts. Without continuous spatial information between the probes one is left to infer the significance of this situation. Such a scenario exists in figure 4 near the downstream end, where by observing the signals from all eight sensors together, one concludes that the different bursts are part of the longer contiguous bulge located in the middle of the figure. In this case, it is

	Bulges	Quiescent zones
Fraction of flow (%)	41.9	35.1
Fraction of I (%)	74.2	3.5
Fraction of $\bar{u}^2$ (%)	87.2	3.2
Fraction of $(\partial u/\partial t)^2$ (%)	83.9	3.8

TABLE 1. Statistics pertaining to the turbulent bulges and irrotational zones.

apparent that the threshold must be less than unity. Of course, as the quiescent zones become longer and the bursts shorter, the likelihood that they are part of the same bulge diminishes. Clearly, the threshold should also be higher than the local value of $\overline{I}$ for the approach to have any significance.

Based on these considerations, a technique utilizing a spatially averaged intermittency was developed. In particular, two spatial averages were used: one of a larger scale to identify when there is a large-scale bulge present,

$$I_{ls}(x, y, z, t) = \frac{1}{n_{ls} n_z} \sum_{i=1}^{n_{ls}} \sum_{k=1}^{n_z} (I_{i,k}(x, y, z, t)) \tag{6}$$

and another of a smaller scale to determine the approximate location of the edge of the bulge (with I_{ss} and n_{ss} replacing I_{ls} and n_{ls} in (6)). Here, I_{ls} is the large-scale spatially averaged intermittency factor, n_{ls} is the number of data points used in time (approximating the streamwise direction) and n_z is the number of probes used in the spanwise direction. I_{ss} and n_{ss} are defined as above, but are of a smaller scale, characteristic of the size of the 'porous' edges of the bulges.

As described above, it is assumed that there is a large-scale bulge present when I_{ls} is near unity and that a quiescent (irrotational) region is present when I_{ls} approaches zero. We thus use I_{ls} to determine when a bulge is present, with a threshold set to an appropriate value. In this case, the threshold used in the determination of the bulges was that the peak value of I_{ls} was greater than 0.70 ($= 1.7\overline{I}$) within the bulge. In order to identify the front and back edges of the bulges the smaller-scale spatially averaged intermittency was used. In particular, once $I_{ss} < 0.30$, it was assumed that the edge had been identified. It was found that the actual value of n_{ls} ($= 19 \sim 1.2L$) was not critical as long as it was chosen to represent the smallest of the large-scale bulges but was not so large that I_{ls} approached the global average at the particular lateral location. We used $n_{ss} = 3$ ($\sim 0.2L$).

3.2. *Statistics of identified bulges and non-turbulent zones*

Using the technique described above, turbulent bulges and quiescent regions were identified with the normal-wire data measured at $y^* = 1.7$ (where $\overline{I} = 0.42$). It was found that 42% of the flow was classified as being bulges of a size greater than $1.2L$, while 35% of the flow was classified as irrotational. The remaining 23% of the flow was unclassified. This could be due to bulges which were only partially aligned with the sensors. Table 1 gives additional statistics relating to these regions showing that the identified bulges captured most of the intermittency and turbulence energy. In contrast, the non-turbulent zones account for very little of the turbulence energy, as expected. Both results indicate that the general classification is good. Interestingly, the fraction of flow classified as 'bulges' is similar to the fraction of the flow occupied by double rollers (e.g. Giralt & Ferré 1993; Vernet *et al.* 1999).

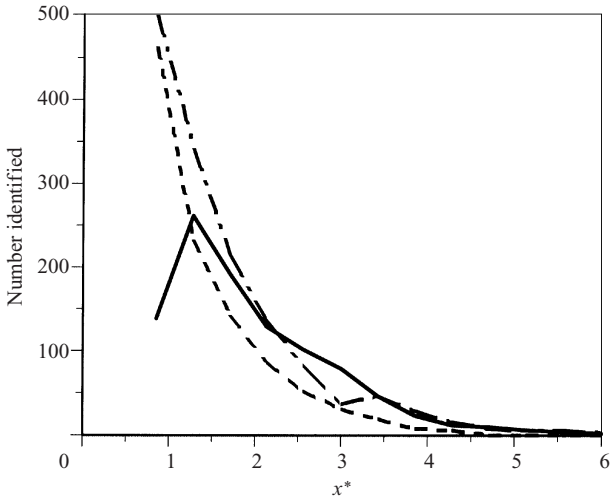

FIGURE 5. Size distribution of large bulges (———) and non-turbulent zone (— - — -) as identified with the bulge identification technique. The distribution of bulges obtained with the single-wire technique (- - -) is also included.

Figure 5 depicts the distribution of bulges and non-turbulent zones by size. The average bulge size near the half-intermittency point is about $x^* = 2.1$. Comparing the present bulge identification technique with that from single-sensor data reported previously (e.g. Kawall & Keffer 1979) shows that the two approaches yield vastly different results. In earlier work it was incorrectly assumed that the turbulence burst rate from a single sensor was an indication of the number of bulges passing the probe per unit time, with each square wave of the turbulence indicator function defining a bulge. With the present data, this single wire approach yields an average bulge size of about $x^* = 0.4$ ($\sim 0.6L$), which is about 20% of the size determined by the multi-sensor technique. This is due to the fact that the indicator function, I, from a single probe is sensitive to undulations of the interface from the largest scales down to those of the size of the sensor measuring volume. Since the interface surface is fractal (Sreenivasan *et al.* 1989), the single-sensor approach will overestimate the number of bulges, being skewed to the smaller scales. The number of large bulges is also underestimated for the same reason.

The number of bulges and non-turbulent zones longer than about $x^* = 1.8$ is equal while for shorter lengths many more non-turbulent zones were identified, especially for $x^* < 1.5$. To investigate this further, a y^* location slightly closer to the wake centreline was examined and it was observed that this situation reversed, consistent with the single-probe results of Kawall & Keffer (1979), until roughly $x^* = 1$. It was also observed that for $x^* = 1$, many more non-turbulent zones were identified. If the smaller bulges can be associated with bulges that have not emerged as far from the fully turbulent core, it could be that these bulges have less 'solidity' and are not identified as often as the non-turbulent zones with the current technique.

As a final comment regarding figure 5, we note that this distribution of bulge sizes and non-turbulent zones should not be fractal since all of the identified events are of a size L or larger. Thus, from this point of view, they should have a fractal dimension similar to the projected area (Sreenivasan *et al.* 1989; Catrakis & Bond 2000).

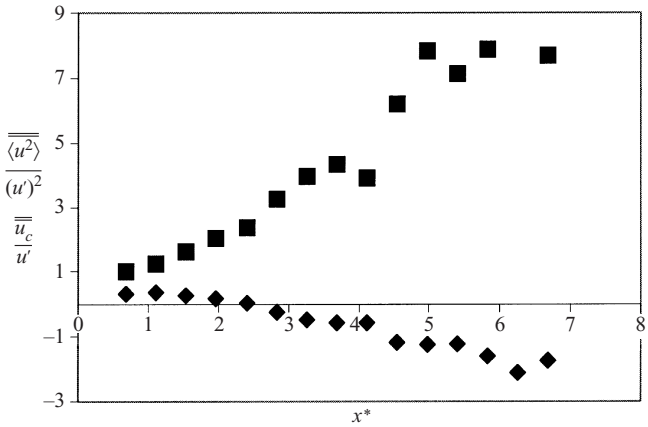

FIGURE 6. Velocity statistics for the bulges identified at $y^* = 1.7$: ◆, $\overline{\overline{u_c}}/u'$; ■, $\overline{\overline{\langle u^2\rangle}}/(u')^2$.

3.3. *Conditional averages of bulges and non-turbulent zones*

Once the bulges and quiescent zones were classified, they were grouped according to size and conditional statistics were obtained. The average bulge size was found to be $x^* = 2.1$, consistent with earlier pattern recognition results. Figure 6 depicts the spatially averaged streamwise velocity fluctuation, $\overline{\overline{u_c}}$, as a function of bulge size, conditioned by $I = 1$ and normalized by the local r.m.s., u', at $y^* = 1.7$. The conditioned mean-square velocity fluctuation is also shown in this figure. For small to average bulges, $\overline{\overline{u_c}}$ is positive, consistent with the rotational flow ($3.4 < x^* < 4.2$) at $y^* = 1.7$ in figure 1(a). For larger bulges, $\overline{\overline{u_c}}$ becomes increasingly negative. The energy associated with the bulges, $\overline{\overline{\langle u^2\rangle}}/(u')^2$, also grows rapidly with bulge size and bulges larger than about $x^* = 3$ have a value of $\overline{\overline{\langle u^2\rangle}}/(u')^2 > 3.0$. In contrast, the quiescent zones are very 'quiet', as expected. Values of $\overline{\overline{u_c}}/u'$ conditioned on $I = 0$ do not vary with zone size and are typically -0.09 (not shown). The typical value of $\overline{\overline{\langle u^2\rangle}}/(u')^2$ is 0.08.

Figures 7–9 show a sample of the results obtained for bulges and non-turbulent zones with streamwise extents of $x^* = 1.7$, 3.0 and 4.2, respectively. These three figures include the isocontours of u_c, obtained at $y^* = 1.7$, and the vectors of (u_c, w_c) at $y^* = 1$. It must be emphasized that these are the average motions occurring simultaneously in time, but physically separated in the lateral direction by $0.7l_0$ ($1.2L$).

Figure 7 depicts the velocity distributions pertaining to bulges and non-turbulent zones of length $x^* = 1.7$. The bulges (figure 7a) have primarily positive velocity fluctuations at $y^* = 1.7$ as indicated by figure 6. Corresponding to these outer motions, the inner motions at $y^* = 1$ have primarily $u_c < 0$, not unlike the region between the two rollers of the horseshoe structure (figure 1). These observations indicate that the motions in the fully turbulent core of the wake associated with outer bulges are the same as those that occur in the mixing jet region at the centre of the double-roller (horseshoe) structure. These motions are well-correlated with outward lateral velocity fluctuations. This is not surprising since it has long been expected that the double-roller portion of the coherent structure forms the base of the turbulent bulges (e.g. Ferré *et al.* 1990; Giralt & Ferré 1993; Kopp, Kawall & Keffer 1995).

Figure 7(b) shows the non-turbulent regions. It is observed that the outer velocity is nearly equal to the local mean velocity since u_c is nearly zero at $y^* = 1.7$. More

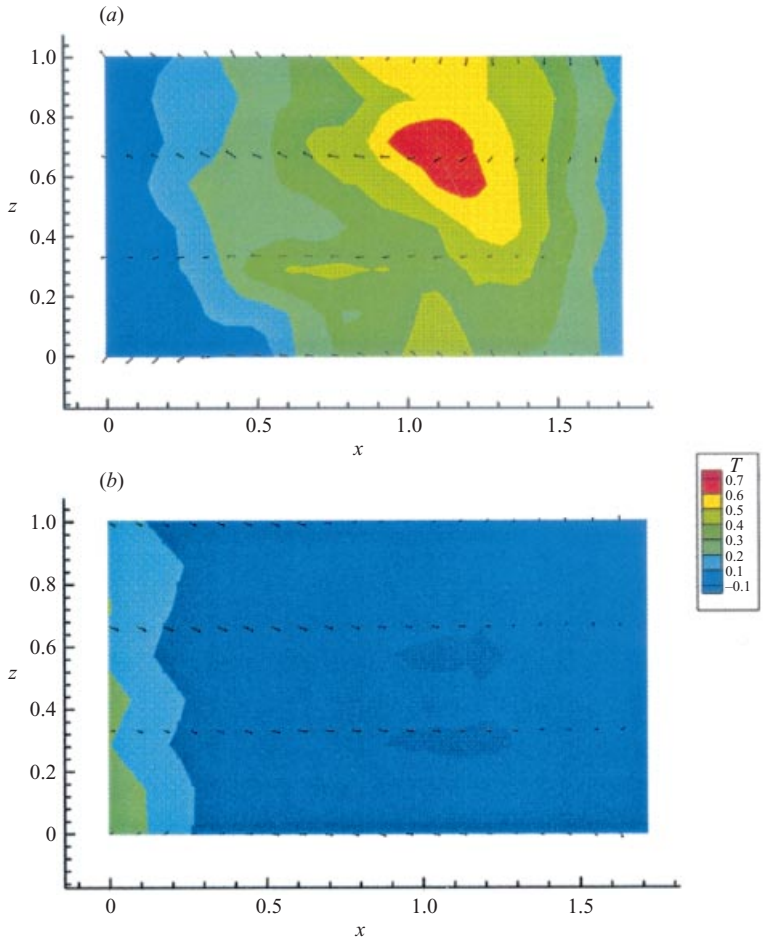

FIGURE 7. Contours of coherent velocities u_c at $y^* = 1.7$ and $\langle u_c, w_c \rangle$ at $y^* = 1.0$ pertaining to events of length $x^* = 1.7$ classified as (a) bulges and (b) non-turbulent zones.

importantly, it is observed that there are positive values of u_c within the turbulent core at $y^* = 1.0$. Comparing figures 1(b) and 7(b) we see that the quiescent zones are similar to either the outer spanwise edges of the double-roller structure or to the back of the double-roller structure, just upstream of the saddle point.

Figures 8 and 9 show the ensemble-averaged velocity fluctuations u_c measured at $y^* = 1.7$ and (u_c, w_c) measured at $y^* = 1$ for bulges and non-turbulent zones of streamwise extent $x^* = 3.0$ and 4.2, respectively. The u_c contours indicate that there are small, slightly positive velocity fluctuations at the leading edge of the bulge. Approximately $1.5l_0$ to $2.5l_0$ upstream, negative streamwise fluctuations of relatively large magnitude are observed. Further upstream, towards the trailing edge of the bulge, the magnitude of u_c is near zero, once again. The inner motions associated with the outer u_c contours are similar to those in figure 7(b), and are dominated by negative values of u_c. These motions have the appearance of the mixing jet motions in figure 1(b). The non-turbulent zone results are presented in figures 8(b) and 9(b). The outer values of u_c are close to zero, as discussed above. The inner motions ($y^* = 1$)

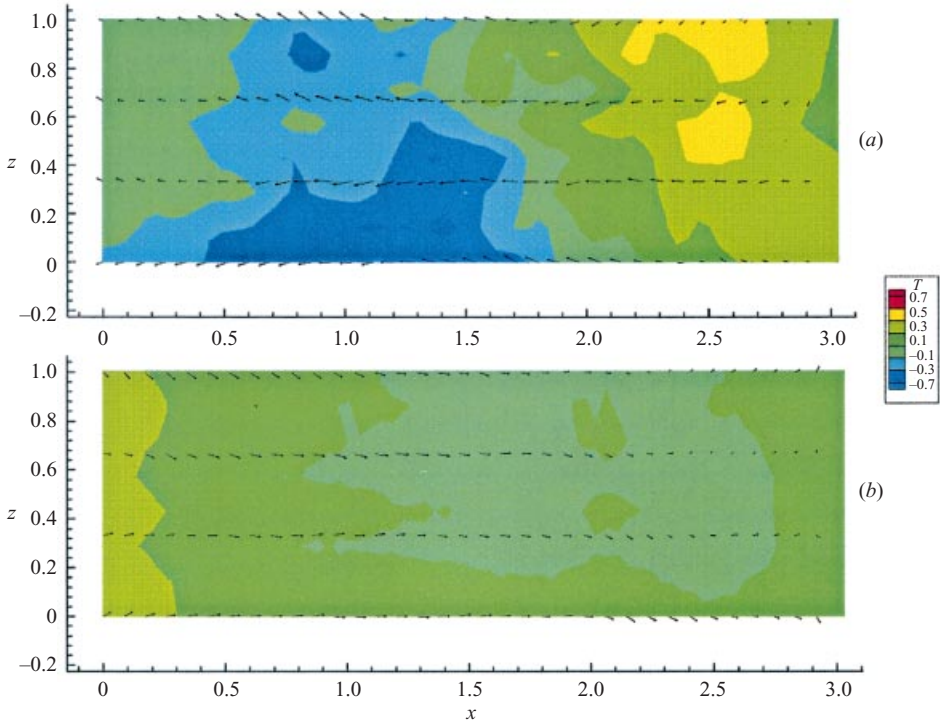

FIGURE 8. As figure 7 but pertaining to events of length $x^* = 3.0$.

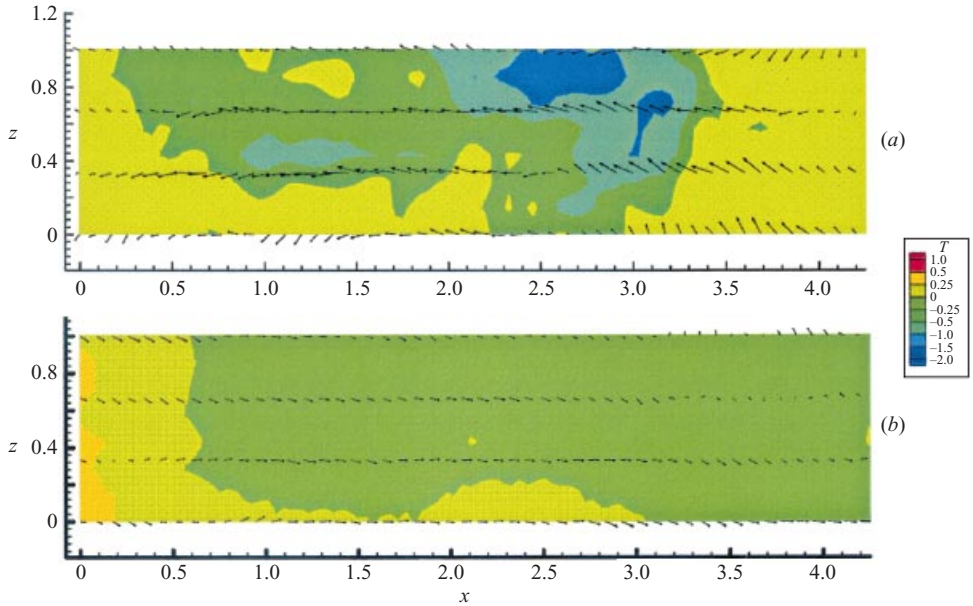

FIGURE 9. As figure 7 but pertaining to events of length $x^* = 4.2$.

are much like those in figure 7(*b*) where positive values of u_c are observed, consistent with the outer portions of the double-roller structure.

3.4. *How the bulges and coherent structures fit together*

It is interesting to compare the average bulge size ($x^* = 2.1$) with the average size of the coherent structures depicted in figure 1. If one examines the (x^*, y^*)-plane at $y^* = 1.7$, it is clear that the size of the straining plus rotational region is about $x^* = 1.8$ in length. Recall that these coherent motions were identified via hotter-to-colder temperature transitions so that the straining region and rotational region are within the hotter fluid while colder fluid is located just upstream of the saddle points. Therefore, based on the results presented so far, it is apparent that both the straining and rotational portions of the coherent structures form the bulges. This result is consistent with the work on the turbulent–non-turbulent interface by LaRue & Libby (1976). These authors found that the upstream edge of the bulge was shear aligned with an angle to the horizontal (i.e. in the x-direction) of 48°. The slope of the straining region in the structure identified by Vernet *et al.* (1999) is similar, as can be observed in figure 1. LaRue & Libby also found evidence of overturning of the downstream face of the bulge with an average angle to the x-coordinate (downstream) direction of 114°. This angle is also consistent with the present coherent structure, although it is difficult to estimate its slope from figure 1 since it is continuously changing in y. Thus, it can be concluded that the horseshoe vortex structure, plus the upstream and downstream straining regions, are the turbulent bulges.

The results of Ferré *et al.* (1990) show that the region near the saddle point at the upstream end of the bulge and the mixing jet has the largest fine-scale activity. In contrast, the outer spanwise edges and the region upstream of the mixing jet have little fine-scale activity, while the downstream straining region has 'average' fine-scale activity. In other words, it is turbulent but corresponds to more recently entrained fluid compared to the 'older' turbulence of the fluid motion emerging from below the upstream straining region in the mixing jet.

Figure 10 shows an idealized sketch of the prototypical (average) bulge overlaid on the motions associated with the inner coherent structure. Note that for $y^* \lesssim 1.0$ the wake is fully turbulent ($\bar{I} \approx 1.0$; see figure 3) and the bulges protrude above this point, as indicated in the sketch. The bulges are made up of the shear-aligned straining region (in yellow) and rotational region (in blue) at the top of the structure, with the slopes of the interface being consistent with the analysis of LaRue & Libby (1976). Entrainment into the wake occurs at the downstream end of the bulge where fluid is 'swept' into the wake and coherent structure, in a way described by Bevilaqua & Lykoudis (1977). The 'randomness' associated with this process allows the coherent motions to extract energy from the entrained fluid, as indicated by the negative isocontours of the production of incoherent turbulence by the coherent motions. These negative production contours, obtained by Vernet *et al.* (1999), overlap with the lower (or downstream) straining region, as indicated in the sketch. At the same time, turbulent fluid is ejected from the core of the wake outwards by the motions induced by the horseshoe vortex. Incoherent turbulence is produced by these motions at the back of the bulge in the upstream straining region, which eventually turns over with the newly entrained fluid at the front.

3.5. *Velocity profiles*

Figure 11 shows the mean velocity profiles associated with the bulges and non-turbulent zones. These profiles were obtained by averaging the values $\langle u^* \rangle$ over x^*

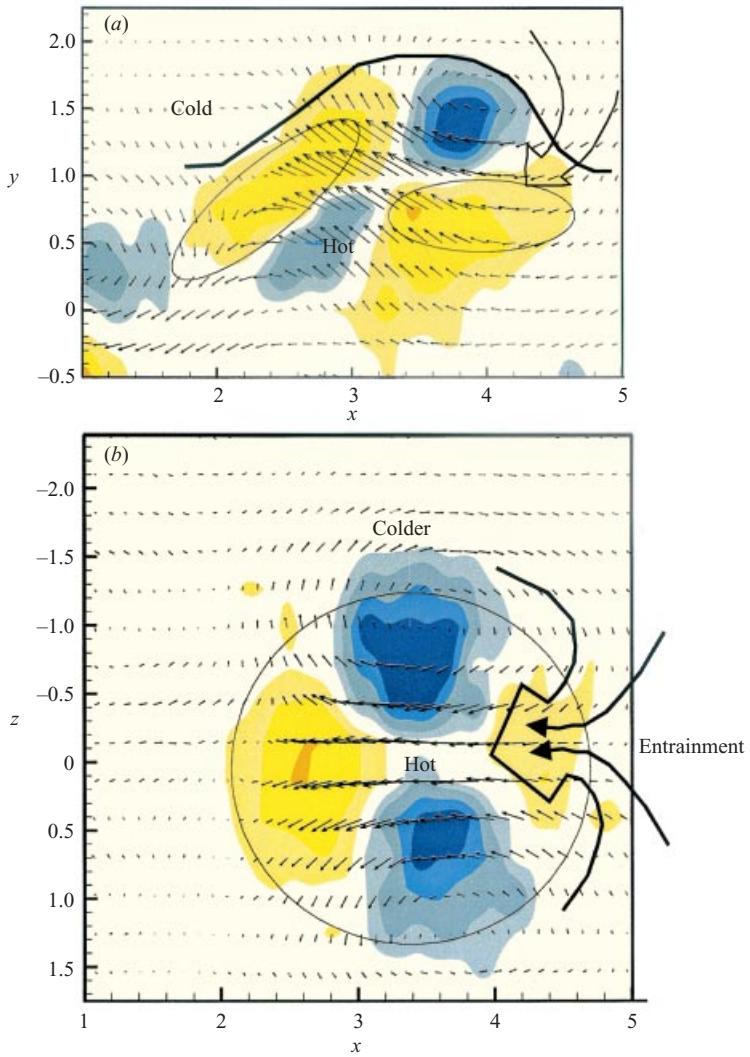

FIGURE 10. Idealized summary sketch of the results of the bulge and non-turbulent zone identification technique at $y^* = 1.7$. The bulges are overlaid on the ensemble-averaged velocity vectors and contours of the second invariant depicted in figure 1. The bulge boundaries also indicate the hot–cold boundaries if the wake were passively 'contaminated' with temperature. Contours of producion of incoherent turbulence by the coherent motion are also sketched in the vertical plane plot as two closed ellipses.

and z^* for a given y^*. Several features can be observed in figure 11. First, it is clear that there is always about the same level of mean shear since the different mean profiles are all approximately parallel. The largest velocities are associated with the non-turbulent zones while the lowest velocities are associated with the largest bulges. These profiles are consistent with the mean velocity profiles associated with the horseshoe structures reported by Vernet *et al.* (1999). The mixing jet portion in the centre of the horseshoe structure has the largest defect, consistent with the profiles for the bulges. The outer regions (i.e. $|z^*| > 1.0$), with positive streamwise velocity fluctuations, are consistent with the non-turbulent zones. Since the turbulence intensity is relatively small compared to the mean defect, it is logical that approximately the

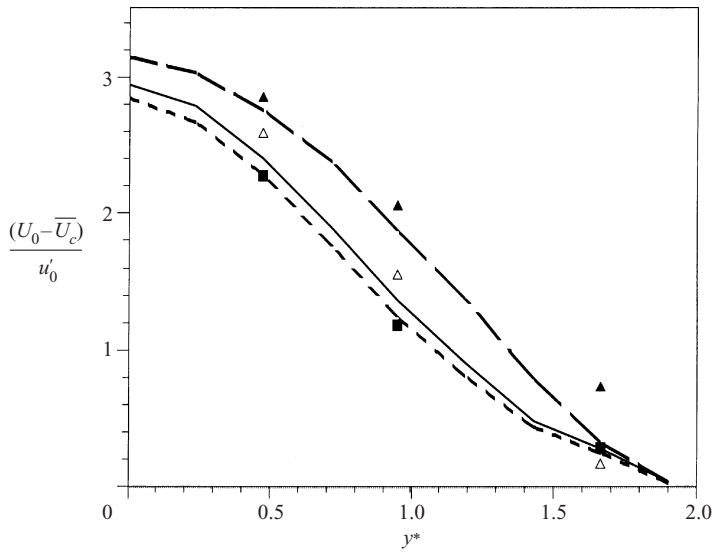

FIGURE 11. Conditional velocity profiles pertaining to bulges of length $x^* = 3.0$ (▲), bulges of length $x^* = 1.7$ (△), non-turbulent zones of length $x^* = 1.7$ (■). The mean velocity profile (——), the spatially averaged coherent velocity u_c in the mixing jet region of the horseshoe structure adapted from Vernet *et al.* (1999) (— — —) and spatially averaged coherent velocity u_c from the outer edges of horseshoe structure adapted from Vernet *et al.* (1999) (- - -) are also shown.

same mean shear is always present. From this perspective, the bulges and coherent structures can be viewed as perturbations from the mean, consistent with the concept of the triple decomposition used in this work.

Phillips (1955) developed a theory for the irrotational velocity fluctuations outside the wake, which has been experimentally validated by several authors (e.g. Fabris 1979; Antonia *et al.* 1987). The main predictions of Phillips' theory that could be evaluated experimentally, according to Antonia *et al.* (1987), are that the mean-square value of the velocity fluctuations should vary as $(y - y_0)^{-4}$ outside the interface and that $v'^2 = u'^2 + w'^2$. These, and other consequences of Phillips' work, were validated both in the region outside of the wake where $\bar{I} = 0$ and for the non-turbulent zones within the wake where $I = 0$. Perhaps the most interesting aspect of the work of Antonia *et al.* (1987) in relation to the current study is that the organized motions outside the wake, which are induced by the coherent motions within the turbulent wake, were examined. These motions too, followed Phillips' theory.

The present experiments were not designed to evaluate Phillips' theory. However, it is interesting to examine the present work in the light of this theory and the results obtained by Antonia and co-workers. To this end, the results obtained by Vernet *et al.* (1999) were re-examined. In particular, the coherent motions (e.g. figure 1) were re-plotted in order to examine the theory. Strictly speaking, these results should have been conditioned on $I = 0$, but since the topology of the bulges relative to the coherent motions is now known, this was not done. Figure 12 shows the results for several locations within, and outside, the horseshoe structure. For points outside the bulge where $u_c > 0$, it appears that the quantity

$$\frac{u_c^2 + w_c^2}{v_c^2} - 1 \tag{7}$$

is asymptotically approaching zero, as required by the theory. We also suspect that,

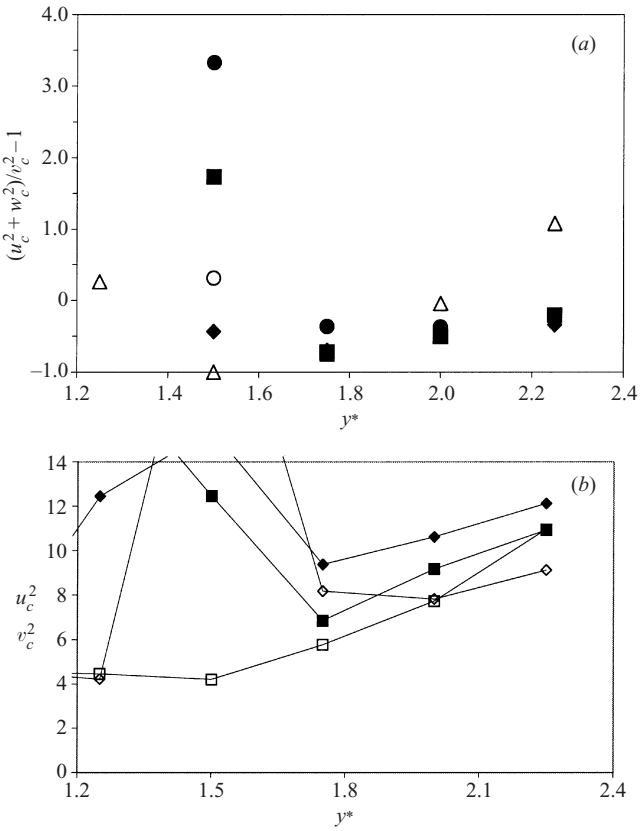

FIGURE 12. Plot of the coherent velocity data of Vernet *et al.* (1999) in coordinates that allow comparison with Phillips' (1955) theory. Open symbols correspond to locations within the average bulge (cf. figure 10) while solid symbols correspond to locations outside the bulge. (*a*) $((u_c^2+w_c^2)/v_c^2)-1$; (*b*) u_c^2(◆) and v_c^2(■).

had the results been conditioned on $I=0$, the results would be clearer. In contrast, for locations within the mixing jet portion of the structure, this does not appear to occur. Similarly, figure 12(*b*) shows that u_c^2 fluctuations vary as $(y-y_0)^{-4}$ outside the bulge area (as marked in figure 10) while those inside it do not follow the trend. Thus, on the whole, the current analysis is consistent with Phillips' theory.

4. Entrainment and bulge time scales

Pope (2000) defines the entrainment time scale for a round jet as

$$\tau_m = \frac{\dot{m}}{U_c(\mathrm{d}\dot{m}/\mathrm{d}x)}, \tag{8}$$

where $\dot{m}$ is the mass flow rate. In the present case we are concerned with the increase in volume of turbulent fluid, not the mass flow rate; however the resulting equation is analogous. The quantity of turbulent fluid passing a streamwise location in the flow per unit width is given by

$$\mu = \int_{-\infty}^{\infty} \bar{I}\,\mathrm{d}y = l_h \int_{-\infty}^{\infty} \bar{I}\,\mathrm{d}y^* = I_1 l_h. \tag{9}$$

Then, the analogous entrainment time scale for wakes can be written as

$$\tau_m = \frac{\mu}{U_0(\mathrm{d}\mu/\mathrm{d}x)}. \tag{10}$$

For round jets there is only a single velocity scale, while for small-deficit plane wakes two velocity scales have to be considered: the free-stream velocity, U_0, which is the bulk convection speed; and the maximum velocity defect, u_0, which is the velocity scale normally used for analyses of self-preservation. From a global point of view, the free-stream velocity is the appropriate choice for entrainment (for the same reason as this velocity is used to convert the time coordinate into the quasi-spatial x-coordinate using Taylor's hypothesis).

Under self-preserving wake flow conditions

$$l_0 = C_l\,(x - x_0)^{1/2}, \qquad u_0 = C_u\,(x - x_0)^{-1/2}. \tag{11}$$

The combination of (9), (10) and (11) with $l_h/l_0 \sim 1.65$ yields

$$\tau_m = \frac{2}{U_0}(x - x_0). \tag{12}$$

The large-scale structures in a wake scale with the mean velocity half-width, l_0, and the maximum velocity defect, u_0, according to Ferré & Giralt (1989*a*). Thus, the application of the eddy time scale proposed by Tennekes & Lumley (1972) to the wake flow yields

$$\frac{\tau_m}{\tau_0} = \frac{2}{U_0}\frac{C_u}{C_l} \sim 10, \tag{13}$$

with $C_u = 1.63$ and $C_l = 0.3$ (see Sreenivasan *et al.* 1989). Thus, the time scale of entrainment is one order of magnitude larger than the nominal eddy time scale. This implies that one should observe several eddies forming and breaking up as one watches the wake grow (say, through a smoke visualization). However, this is not the case, since wakes (and the other fully developed free shear flows) appear to be frozen over large streamwise distances. Therefore, it is worth revisiting the eddy time scale. In fact, the actual scale of eddies is about l_0 (figure 1) while a better velocity scale would be $0.1u_0$, since $u'/u_0 \sim 0.3$ and $\overline{\overline{u}}_c/u' \sim 0.3$ (see figure 4 in Vernet *et al.* 1999 and § 6). This leads to a new time scale

$$\tau_{eddy} \sim \frac{l_0}{0.1u_0} = 10\frac{C_l}{C_u}(x - x_0) \tag{14}$$

so that

$$\frac{\tau_m}{\tau_{eddy}} \sim \frac{1}{5}\frac{C_u}{C_l}\frac{1}{U_0} \sim 1. \tag{15}$$

This is consistent with both observations of the growth of wakes via flow visualization (where wakes appear frozen over long streamwise distances with the bulges emerging like 'mushrooms') and also with the fact that the turbulent velocity fluctuations can be viewed as a perturbation to the mean velocity field. This implies that the large-scale eddies are long-lived, consistent with the mechanism of entrainment.

5. The entrainment mechanism in the far wake

If the entrainment mechanism in the far region is related to the KH instability, then it is also connected to the origin of the far-wake structures. This latter topic

has been a contentious issue in the literature with two points of view put forward: the far-wake structures (i) being formed via the KH instability which re-asserts itself after the Kármán vortices decay and disappear (e.g. Cimbala, Nagib & Roshko 1988), or (ii) originating in the near wake, evolving directly from the shed vortices (e.g. Hussain & Hayakawa 1987). Interestingly, Wygnanski *et al.* (1986) propose a solution, indicating that the perturbations required for the instability mechanism may be the structures themselves. In any case, the present results will now be discussed to determine compatibility with the KH instability.

5.1. *Stage* 1 – *growth*

As described earlier, both the KH instability and Townsend's growth–decay cycle begin with a relatively thin wake. In terms of the present work, this should correspond to the relatively long non-turbulent zones detected at the outer probes ($y^* = 1.7$), with turbulent flow below. Since the inner turbulent flow is 'older' and relatively well-mixed, it should travel on average at about the local mean velocity since the flow would be structureless, or have structures without preferred alignment. (However, Townsend (1976) indicates that the double rollers are part of the 'main turbulent motion' which exists below the (smooth) interface. This structure would also lead to spatially averaged streamwise velocity fluctuations close to zero, and a Reynolds shear stress due to their inclination.) The outer flow should be travelling nearly at the free-stream speed which implies positive streamwise fluctuations for say $1.5 \lesssim y^* \lesssim 2.0$. This scenario does not agree with the present experiments. Figures 8 and 9 show that the streamwise fluctuations in the outer region ($y^* = 1.7$) are nearly zero or slightly negative while positive streamwise fluctuations occur in the inner region ($y^* = 1.0$). Ferré *et al.* (1990) and Vernet *et al.* (1999) showed that these positive streamwise fluctuations are associated with less-fine-scale turbulence and, therefore, relatively 'newer' wake fluid. Thus, the long non-turbulent zones do not seem to be associated with the initial stages of the KH instability or the growth–decay cycle. Given the similarity of the velocity profiles (figure 7) and ensemble-averaged velocities with the outer portion of the double rollers (cf. figure 1*b* for $|z^*| > 1.0$), it appears that the long irrotational zones are part of the motions associated with the double roller/horseshoe.

5.2. *Stage* 2 – *overturning*

In the next stages of the KH instability and the growth–decay cycle there is growth of the outer bulges, which roll up (or turn over) with entrainment ensuing. This stage is consistent with the results described in detail in § 3 and summarized by figure 10. The question arises as to whether the turning over is like the well-known 'cat's eye' (e.g. see figure 4 in Sreenivasan *et al.* 1989) or like the 'sweeping in' described by Bevilaqua & Lykoudis (1977) with their flow visualization. The difference between these two descriptions appears to be more of degree than of physics, as discussed in the introduction.

In either case, it appears that the structures are maintained for long streamwise extents, as observed by Bevilaqua & Lykoudis (1977), for several reasons beyond those given in § 4. Wygnanski *et al.* (1986) suggested that the perturbation required for instability was the structures themselves. This provided the fundamental mechanism for how the initial conditions at the wake generator are propagated into the far wake. This is also consistent with two additional factors. First, turbulence levels in the far field are rather low compared to the maximum defect. For example, the maximum root-mean-square (r.m.s.) streamwise velocity is about 30% of the maximum mean defect (Townsend 1976). Given that peak coherent velocity fluctuations associated with

the coherent structures are usually about twice the r.m.s., there is always a significant velocity defect profile present even if it is not precisely similar to the shape of the mean velocity profile (figure 7). This is consistent with the far-wake structures being perturbations from the mean. Nevertheless, there are some difficulties with this argument, as put forward by Vernet *et al.* (1999), since the mean shear should pull apart these structures rather rapidly. We suspect that the continual entrainment of new fluid along with the long time scales of the entrainment eddies prevents this by allowing the structures to come into equilibrium with the conditions present at the new location where they have been advected by extracting energy from the newly entrained, faster moving fluid.

5.3. *Stage* 3 – *filling*

The growth–decay cycle suggests that the troughs are filled in and the wake returns to the quiescent stage after the bulges have overturned, while it has approximately doubled in width according to Townsend (1976). In the present work, this would imply that all probes are imbedded in turbulent flow and long bulges would be identified. One would expect that the motions observed in this case would be like the inner motions for the first-stage quiescent period when long non-turbulent zones are identified. This, in fact, does not occur. For long bulges, the inner motions at $y^* = 1.0$ have strong negative streamwise fluctuations in contrast to the positive streamwise fluctuations for the inner motions when long non-turbulent zones are identified. Thus, no evidence of the filling-quiescent stage is found in the present work.

5.4. *Discussion*

Townsend (1979) and Ferré & Giralt (1989*a*) both discussed the grouping of the large-scale eddies within the far region of a turbulent wake. Townsend (1979) observed groups of about three while Ferré & Giralt found the groupings to be more random since there was no preferred spanwise location for the vortices. Thus, if the bulge/entrainment eddy locations are random in the spanwise direction (as implied by mean two-dimensionality of the flow), they could align occasionally to form very long bulges with engulfment only occurring at the leading eddy, as sketched by Ferré *et al.* (1990). This would lead to negative streamwise velocity fluctuations in the core, consistent with those in the mixing jet region. If the horseshoe vortices were all exactly the same size and strength and had precisely the same lateral location, one would expect distinct peaks in the size distribution depicted in figure 5 corresponding to groups of $1, 2, 3, \ldots, n$ bulges in a row. The random nature of the size, strength and location variables (with a definable mean) is consistent with the distribution given in figure 5. Yao & Paschal (1994) show PIV images of the wake of an airfoil where large changes in the vortex location are observed. In particular, they show a large bulge that has emerged significantly from the centre of the wake and looks like that in our figure 1. Thus, the long bulges are most likely due to structures that have emerged much further from the centreline and also to several structures occurring sequentially in a group, much like Kim & Adrian's (1999) 'very large scale motions' observed in turbulent boundary layers.

6. Propagation velocities

Corrsin & Kistler (1955) examined the propagation velocity of the turbulent–non-turbulent interface and found it to be the Kolmogorov velocity. This velocity, together with the true area of the interface, allows the calculation of the momentum flux across the wake boundary (see Sreenivasan *et al.* 1989). In contrast, Townsend (1976), Turner

(1986), Sreenivasan *et al.* (1989) and others have looked at the propagation speed from the global momentum balance point of view and estimated entrainment velocities to be proportional to the velocity scale, in this case u_0. Turner (1986) examined the implications of this 'entrainment hypothesis'. The entrainment velocity is typically defined as

$$V_e = \frac{\mathrm{d}}{\mathrm{d}x} \int_{-\delta}^{\delta} \overline{U}\, \mathrm{d}y, \tag{16}$$

which clearly depends on the similarity of the whole flow. Thus, it is interesting to relate a typical velocity associated with the large eddies with V_e.

Figure 5 and table 1 both show that the contribution to the turbulence intensities at the outer (intermittent) edge of the wake is primarily due to the bulges and that the velocities associated with these bulges correspond directly to the mixing jet portion of the horseshoe structures. Thus, the turbulence intensity profiles, and their similarity as the flow develops, depend on the bulges. This is consistent with the fact that Kopp *et al.* (1995) were able to predict many aspects of the wake spread using a simple vortex model and rapid distortion theory when a uniform, irrotational strain was applied to a far wake. Thus, the propagation speed of the front (interface) should also depend on the large-scale entrainment eddies.

As mentioned above, figure 5 has shown that the typical velocity fluctuations in the bulges (at $y^* = 1.7$) are positive for the average bulge. For larger bulges, which have emerged further, the streamwise fluctuations are strongly negative, very energetic and correspond to the mixing jet region of the horseshoe vortices, closer to those at $y^* = 1$ in figure 1. Examining figure 4 in Vernet *et al.* (1999), typical velocity fluctuations averaged over the entire mixing jet region are $0.5u_0'$ where u_0' is the streamwise r.m.s. velocity at $y^* = 1$ (which is close to the maximum value). This translates to about $1.4u'$, where u' is the local r.m.s. velocity. For the present flow, the ratio u_0'/u_0 is about 0.3 and the average velocities associated with the mixing jets/bulges are about $0.5u_0'/u_0 = 0.15u_0$. This is three times smaller than the entrainment velocity, $V_e = 0.46u_0$ determined by Sreenivasan *et al.* (1989) using equation (16) above for self-preserving cylinder wakes.

It has typically been argued (e.g. Corrsin & Kistler 1995) that the turbulent fluctuations close to the interface are generally of a similar magnitude to those in the fully turbulent core of the flow. Thus, the conditional, turbulent velocity fluctuations should be similar to the Kolmogorov velocity, v_k. Sreenivasan *et al.* (1989) pointed out that the ratio V_e/v_k should be equal to the true (fractal) interface area divided by the projected area,

$$\frac{A_t}{A_p} = \left(\frac{\eta}{L}\right)^{2-D}, \tag{17}$$

where $D = 7/3$ is approximately constant for a wide range of turbulent flows, but varies slightly for $Re_D < 10\,000$. Estimating the dissipation via u'^3/L, results in $\eta \sim 0.6\,\mathrm{mm}$ and the area ratio is about 3.3. This could be considered remarkably close to the velocity ratio, given the many experimental uncertainties involved in the calculation.

7. Conclusions

Turbulent bulges and non-turbulent zones have been identified in the far-wake region of a circular cylinder and related to the prototypical coherent structure in this

region. It is observed that inflow occurs from the sides and downstream edge of the three-dimensional bulges. The bulges, which protrude above $y^* = 1.0$, are made up of the top of the horsehoe vortex and an upstream straining region. The rear (upstream) edge is shear-aligned, while the downstream edge is not, consistent with the work of LaRue & Libby (1976). The bulge/coherent structure extracts energy from the newly entrained fluid, helping to maintain it for long streamwise distances. Incoherent turbulence is produced at the upstream end of the bulge in the shear-aligned straining region.

The implications of the present work for the KH instability and Townsend's growth–decay cycle as models of entrainment have been examined. It was found that the bulges conform to the overturning stage, but no evidence is found for the quiescent periods at the beginning and end of the cycle. It is speculated that the structures are maintained or frozen, for extremely long distances downstream, by the instability mechanism, as implied by Wygnanski *et al.* (1986), with the perturbations required for the instability mechanism being the structures themselves. In this way, the initially shed vortices do not disappear completely, but rather evolve into the horseshoe vortices in the far region. The growth of the wake, and its overall similarity, is due to the emergence of these bulges from the fully turbulent core.

Thanks are accorded to Dr A. Vernet for his assistance with some of the plots and analysis. This work was financially supported by DGICYT projects PB96-1011 and PPQ2000-1339, CIRIT project 1998SGR-00102, NATO Collaborative Research Grant 960142. Computing support was provided by the University of Western Ontario through the VP(R) program. G. A. Kopp gratefully acknowledges the support of the Universitat Rovira i Virgili and NSERC (Canada) during the portion of the work carried out in Tarragona, and also the ongoing support of the Canada Research Chairs Program.

REFERENCES

Antonia, R. A., Browne, L. W. B., Bisset, D. K. & Fulachier, L. 1987 A description of the organized motion in the turbulent far wake of a cylinder at low Reynolds number. *J. Fluid Mech.* **184**, 423–444.

Antonia, R. A., Shah, D. A. & Browne, L. W. B. 1987 The organized motion outside a turbulent wake. *Phys. Fluids* **30**, 2040–2045.

Bevilaqua, P. M. & Lykoudis, P. S. 1977 Some observations on the mechanism of entrainment. *AIAA J.* **15**, 1194–1196.

Catrakis, H. J. & Bond, C. L. 2000 Scale distributions of fluid interfaces in turbulence. *Phys. Fluids* **12**, 2295–2301.

Caulfield, C. P. & Peltier, W. R. 2000 The anatomy of mixing transition in homogeneous and stratified free shear layers. *J. Fluid Mech.* **413**, 1–47.

Cimbala, J. M., Nagib, H. M. & Roshko, A. 1988 Large structure in the far wakes of two-dimensional bluff bodies. *J. Fluid Mech.* **190**, 265–298.

Corrsin, S. & Kistler, A. L. 1955 Free-stream boundaries of turbulent flows. NACA report 1244.

Dimotakis, P. E. 2000 The mixing transition in turbulent flows. *J. Fluid Mech.* **409**, 69–98.

Fabris, G. 1979 Conditional sampling study of the turbulent wake of a cylinder. Part 1. *J. Fluid Mech.* **94**, 673–709.

Ferré, J. A. & Giralt, F. 1989*a* Pattern recognition analysis of the velocity field in plane turbulent wakes. *J. Fluid Mech.* **198**, 27–64.

Ferré, J. A. & Giralt, F. 1989*b* Some topological features of the entrainment process in a heated turbulent wake. *J. Fluid Mech.* **198**, 65–77.

Ferré, J. A. Mumford, J. C., Savill, A. M. & Giralt, F. 1990 Three-dimensional large-eddy motions and fine-scale activity in a plane turbulent wake. *J. Fluid Mech.* **210**, 371–414.

Giralt, F. & Ferré, J. A. 1993 Structure and flow patterns in turbulent wakes. *Phys. Fluids* A **5**, 1783–1789.

Grant, H. L. 1958 The large eddies of turbulent motion. *J. Fluid Mech.* **4**, 149–190.

Hedley, T. B. & Keffer, J. F. 1974 Turbulent/non-turbulent decisions in an intermittent flow. *J. Fluid Mech.* **64**, 625–644.

Hussain, A. K. M. F. 1983 Coherent structures – reality and myth. *Phys. Fluids* **26**, 2816–2850.

Hussain, A. K. M. F. & Hayakawa, M. 1987 Education of large-scale organized structures in a turbulent plane wake. *J. Fluid Mech.* **180**, 193–229.

Kawall, J. G. & Keffer, J. F. 1979 Interface statistics of a uniformly distorted heated turbulent wake. *Phys. Fluids* **22**, 31–39.

Kawall, J. G. & Keffer, J. F. 1980 Techniques of generating turbulence indicator functions. *Anales Fisica* **76**, 253–260.

Kim, K. C. & Adrian, R. J. 1999 Very large-scale motion in the outer layer. *Phys. Fluids* **11**, 417–422.

Kopp, G. A., Kawall, J. G. & Keffer, J. F. 1995 The evolution of the coherent structures in a uniformly distorted plane turbulent wake. *J. Fluid Mech.* **291**, 299–322.

LaRue, J. C. & Libby, P. A. 1976 Statistical properties of the interface in the turbulent wake of a heated cylinder. *Phys. Fluids* **19**, 1864–1875.

Mumford, J. C. 1983 The structure of the large eddies in fully developed turbulent shear flows. Part 2. The plane wake. *J. Fluid Mech.* **137**, 447–456.

Ottino, J. M. 1989 *The Kinematics of Mixing: Stretching, Chaos and Transport*. Cambridge University Press.

Phillips, O. M. 1955 The irrotational motion outside a free turbulent boundary. *Proc. Camb. Phil. Soc.* **51**, 220–229.

Pope, S. B. 2000 *Turbulent Flows*. Cambridge University Press.

Prandtl, L. & Tietjens, O. G. 1934 *Fundamentals of Hydro- and Aeromechanics*. United Engineers Trustees.

Sreenivas, K. R. & Prasad, A. K. 2000 Vortex-dynamics model for entrainment in jets and plumes. *Phys. Fluids* **12**, 2101–2107.

Sreenivasan, K. R. 1991 Fractals and multifractals in turbulence. *Annu. Rev. Fluid Mech.* **23**, 539–600.

Sreenivasan, K. R., Ramshankar, R. & Meneveau, C. 1989 Mixing, entrainment and fractal dimensions of surfaces in turbulent flows. *Proc. R. Soc. Lond.* A **421**, 79–108.

Tabatabai, M., Kawall, J. G. & Keffer, J. F. 1989 Choice of the threshold in a velocity-based conditional sampling procedure. *Phys. Fluids* A **1**, 307–311.

Tennekes, H. & Lumley, J. L. 1972 *A First Course in Turbulence*, p. 68. MIT Press.

Townsend, A. A. 1966 The mechanism of entrainment in free turbulent flows. *J. Fluid Mech.* **26**, 689–715.

Townsend, A. A. 1976 *The Structure of Turbulent Shear Flow*, 2nd edn. Cambridge University Press.

Townsend, A. A. 1979 Flow patterns of large eddies in a wake and in a boundary layer. *J. Fluid Mech.* **95**, 515–537.

Turner, J. S. 1986 Turbulent entrainment: the development of the entrainment assumption, and its application to geophysical flows. *J. Fluid Mech.* **173**, 431–471.

Vernet, A., Kopp, G. A., Ferré, J. A. & Giralt, F. 1999 Three-dimensional structure and momentum transfer in a turbulent cylinder wake. *J. Fluid Mech.* **394**, 303–337.

Villermaux, E. & Innocenti, C. 1999 On the geometry of turbulent mixing. *J. Fluid Mech.* **393**, 123–147.

Warhaft, Z. 2000 Passive scalars in turbulent flows. *Annu. Rev. Fluid Mech.* **32**, 203–240.

Wygnanski, I., Champagne, F. & Marasli, B. 1986 On the large-scale structures in two-dimensional, small-deficit, turbulent wakes. *J. Fluid Mech.* **168**, 31–71.

Yao, C. & Paschal, K. 1994 PIV measurements of airfoil wake-flow turbulence statistics and turbulent structures. *AIAA Paper* 94-0085.